Combustion and Flame 207 (2019) 379–390

Contents lists available at ScienceDirect

Combustion and Flame

journal homepage: www.elsevier.com/locate/combustflame

Multi-isotopologue laser absorption spectroscopy of carbon monoxide for high-temperature chemical kinetic studies of fuel mixtures

Daniel I. Pineda*, Fabio A. Bendana, Kevin K. Schwarm, R. Mitchell Spearrin

Department of Mechanical and Aerospace Engineering, University of California, Los Angeles, Los Angeles, CA 90095, United States

ARTICLE INFO

Article history:
Received 28 March 2019
Revised 16 May 2019
Accepted 16 May 2019

Keywords:
Isotopic labeling
Shock tube kinetics
Absorption spectroscopy

ABSTRACT

A laser absorption diagnostic technique, probing the mid-infrared vibrational bands of $^{12}C^{16}O$ and $^{13}C^{16}O$ near 4.9 μm, was developed for sensitive multi-isotopologue temperature and concentration measurements in high-temperature gaseous systems. Transitions in each of the P-branches of the fundamental bands of $^{12}C^{16}O$ and $^{13}C^{16}O$ were chosen based on absorption linestrength, relative spectral isolation, and temperature sensitivity. Five total rovibrational transitions are spectrally-resolved over a $\sim$1.2 cm^{-1} domain using a 50 kHz triangle scan function with a distributed-feedback quantum cascade laser, yielding a 100 kHz effective measurement rate of both isotopologues and respective temperatures, independent of mixture composition. In addition, relevant broadening parameters for the P(0,22) transition of $^{13}C^{16}O$ near 2007.8767 cm^{-1} were measured to enable higher time resolution ($>$1 MHz) measurements using fixed-wavelength methods. Time-resolved multi-isotopologue thermometry performance was validated in a shock tube over a range of temperatures (1100–2400 K) relevant to combustion kinetics investigations. The technique is utilized in shock-heated oxidation experiments with isotopically labeled fuel mixtures, simultaneously measuring both carbon monoxide isotopologues throughout the reactions. To the authors' knowledge, these results demonstrate the first use of carbon isotope labeling with laser absorption spectroscopy to observe distinct competitive oxidation among different fuel components.

1. Introduction

Optical sensing of carbon monoxide (CO) is important for a variety of applications, including environmental health safety monitoring and combustion efficiency characterization. In regards to combustion, CO is a significant intermediate species, measurements of which are often used to validate and develop chemical kinetic models for combustion applications [1]. Particularly, laser absorption spectroscopy (LAS) is a common method for quantitatively measuring concentration of combustion species—including CO [2–9]—at high time resolution during combustion reactions behind reflected shock waves, providing valuable experimental constraints on kinetic models of hydrocarbon decomposition and oxidation. Most of these measurements have been made using 'neat' mixtures comprising a single fuel; practical fuels used in real combustion devices are typically blends of many different hydrocarbons with similar intermediates and products [10]. During the initial fuel pyrolysis prior to oxidation, these fuel molecules tend to decompose into a small number of similar C_1–C_4 intermediates, the kinetics of which largely dictate the evolution of the rest of the reaction [11,12]. These intermediates compete with one another in oxidation reactions, making it difficult to characterize the contributions of a particular fuel component on overall combustion behavior when probing a single kinetic parameter.

To experimentally contrain complex kinetics models, an increased number of parameters must be measured in controlled studies. Deliberately labeled isotopologues, particularly those that contain isotopes of hydrogen atoms, are commonly used in physical organic chemistry research to distinguish reaction pathways [13,14]. Here we focus on carbon as a shared element in fuels and the intermediate CO, which can be readily measured by infrared absorption. Roughly 1.1% of all carbon on Earth is ^{13}C [15,16], making it one of the more common stable isotopes available for use in isotopic tagging techniques [13,15] and representing an opportunity for combustion kinetics investigations [14]. Accordingly, this work targets the infrared absorption spectra of the two most abundant isotopologues of CO, $^{12}C^{16}O$ and $^{13}C^{16}O$, as shown in Fig. 1.

In this article, we describe a laser absorption sensor that simultaneously probes the distinct spectra of $^{12}C^{16}O$ and $^{13}C^{16}O$ (abbreviated in this work as ^{12}CO and ^{13}CO, respectively) to recover

* Corresponding author.
E-mail address: dipineda@ucla.edu (D.I. Pineda).

https://doi.org/10.1016/j.combustflame.2019.05.030
0010-2180/

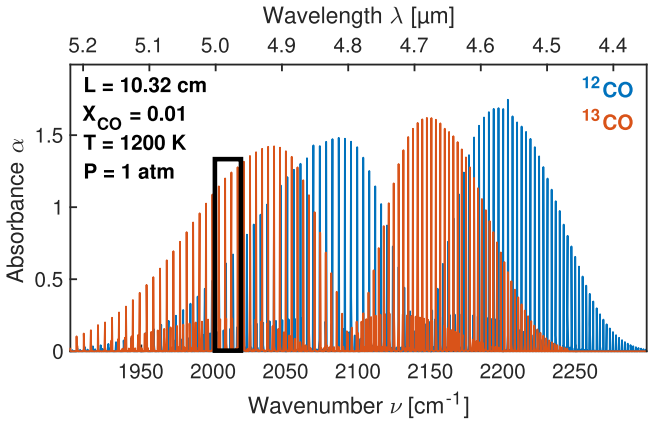

Fig. 1. Simulated spectra of ^{12}CO and ^{13}CO calculated at conditions relevant to combustion. Targeted spectral region outlined in black. Spectral line parameters taken from HITEMP database [17]. (For the interpretation of references to color in this figure, the reader is referred to the web version of this article.)

mole fraction and temperature in high-temperature shock tube kinetics studies. The technique is coupled with isotopic labeling of fuel components with either a ^{12}C or ^{13}C to discern the influence of specific fuels on the aggregate combustion behavior of fuel mixtures. We present the sensor development by first discussing the influence of isotopic labeling and substitution on molecular spectra in the context of wavelength selection. After establishing the theoretical foundations of the technique, we detail our experimental methodology, including the optical setup, experimental apparatus, and data processing techniques required to obtain temperatures and mole fractions from our absorption measurements. We describe both a scanned-wavelength direct absorption (scanned-DA) method for simultaneous multi-isotopologue detection and a fixed-wavelength direct absorption (fixed-DA) method for high-speed sensing of ^{13}CO. Validation measurements in non-reactive shock tube experiments are followed by demonstration of the capabilities of multi-isotopologue LAS in reacting mixtures of isotopically labeled fuels at high temperatures. The paper concludes with an example analysis highlighting the unique utility of the technique to help distinguish chemical kinetic pathways.

2. Background and theory

This section discusses the relevant background for laser absorption spectroscopy (LAS) with isotopologues of carbon monoxide for high-temperature chemical kinetic studies.

2.1. Isotopic effects on molecular spectra

Absorption spectra for ^{12}CO and ^{13}CO are shown in Fig. 1. For a diatomic molecule approximated as a harmonic oscillator, the fundamental vibrational frequency ω_e is dependent on the bond stiffness k_s and the reduced molecular mass μ [18]:

$$\omega_e \propto \sqrt{\frac{k_s}{\mu}} \tag{1}$$

The spacing between rovibrational transition frequencies, set by the rotational constant, B, is also dependent on μ:

$$B \propto \frac{1}{\mu} \tag{2}$$

For an isotopologue, changes in nuclear mass of a molecule without a change in the number of protons does not strongly affect bond length r_e or the bond stiffness k_s [19]. As a result, ω_e changes as μ changes; an increase in reduced mass shifts the center of the overall vibrational band to lower frequencies, seen in Fig. 1, by about 50 cm^{-1} for CO. Additionally, the rotational constant B is also affected—albeit less obviously—as seen in Fig. 1, in which the line spacing between rovibrational transitions reduces by approximately 0.17 cm^{-1}. These isotopic substitution effects provide a basis for understanding the ability to spectrally distinguish ^{12}CO and ^{13}CO isotopologues using LAS, and provides a basis for their independent detection in oxidation experiments of isotopically labeled fuels.

2.2. Laser absorption spectroscopy

Laser absorption spectroscopy (LAS) relates the attenuation of light in a gas medium to thermophysical properties such as temperature, pressure, and concentration. The theory of LAS is documented in detail in the literature [19], and so only important results are briefly outlined here for reader comprehension. The Beer–Lambert law in Eq. (3) defines the spectral absorbance α_ν in a uniform medium of pathlength L [cm] for a specific frequency ν as a function of the ratio of incident light intensity, I_0, and transmitted light intensity, I_t:

$$\alpha_\nu = -\ln\left(\frac{I_t}{I_0}\right)_\nu = PX_{\text{abs}}S_i(T)\varphi_i(\nu)L \tag{3}$$

The spectral absorbance α_ν depends linearly on total pressure P [atm], mole fraction of absorbing species X_{abs}, line strength $S_i(T)$ [cm^{-2}/atm] for rovibrational transition i at temperature T [K], lineshape function $\varphi_i(\nu)$ [cm] and the pathlength L [cm]. $\varphi_i(\nu)$ is the only variable with a spectral dependence, and varies depending on the gas temperature as well as partial pressures of different collision partners. In scanned-wavelength direct absorption, it is possible to scan across the entire spectral domain of transition i to resolve the lineshape profile $\varphi_i(\nu)$, albeit at the expense of some temporal resolution. Total absorbance area for a single isolated transition can then be calculated by integrating absorbance in the spectral domain:

$$A_i = \int_{-\infty}^{\infty} \alpha_\nu d\nu = PS_i(T)X_{\text{abs}}L \tag{4}$$

which eliminates the dependence on the lineshape function $\varphi_i(\nu)$ ($\int_{-\infty}^{\infty}\varphi_i(\nu)d\nu = 1$). This is usually achieved in practice by fitting an assumed lineshape function to the spectra. The ratio R of two absorbance areas associated with two rovibrational transitions A and B eliminates dependence on mole fraction, pressure, and pathlength:

$$R = \frac{A_A}{A_B} = \frac{S_A(T)}{S_B(T)} = f(T) \tag{5}$$

Temperature-dependent linestrengths $S_A(T)$ and $S_B(T)$ can be calculated from reference-temperature linestrengths $S_A(T_0)$ and $S_B(T_0)$, which for the transitions used in this work are known in the HITRAN database [20] to within 2% uncertainty (For more detail, refer to Appendix A). Thus, by simultaneously resolving at least two transitions for a given species and calculating their absorbance areas, the temperature of the gas can be inferred without requiring detailed information about the broadening parameters of the lineshape, resulting in a measurement independent of gas composition and pressure. Once T is known, Eq. (4) can be used to determine mole fraction, assuming that pressure is measured independently. Taking the derivative of the expressions for $S_i(T)$ with respect to temperature, the temperature-sensitivity of R can be approximated as [19]:

$$\left|\frac{dR/R}{dT/T}\right| \approx \left(\frac{hc}{k_B}\right)\frac{\left|E_A'' - E_B''\right|}{T} \tag{6}$$

where h [J·s] is the Planck constant, c [cm/s] is the speed of light, k_B [J/K] is the Boltzmann constant, and E_i'' [cm^{-1}] is the lower state energy associated with rovibrational transition i. Noteworthy in Eq. (6) is that temperature sensitivity is greater for transition pairs which have greater differences in lower state energy; this influences the line selection process.

In this work, we demonstrate a sensor utilizing both scanned-wavelength direct-absorption (scanned-DA) and fixed-wavelength direct-absorption (fixed-DA) techniques, the latter of which require additional line broadening parameters pertaining to the lineshape function $\varphi_i(\nu)$, but which enables faster measurements. In both techniques, we model $\varphi_i(\nu)$ using the Voigt lineshape profile, a convolution of Lorentzian and Gaussian profiles which describes collisional and temperature line broadening effects, respectively [19]. The value of $\varphi_i(\nu)$ at the transition linecenter, $\nu_{i,0}$, can be calculated by:

$$\varphi_i(\nu_{i,0}) = \frac{2}{\Delta\nu_D}\sqrt{\frac{\ln 2}{\pi}}\exp\left(a^2\right)[1-\mathrm{erf}(a)] \tag{7}$$

where:

$$a = \frac{\sqrt{\ln 2}\Delta\nu_c}{\Delta\nu_D} \tag{8}$$

In this profile, the thermal broadening of the line is characterized by a Doppler width $\Delta\nu_D$ [cm^{-1}],

$$\Delta\nu_D = \nu_{i,0}\left(7.1629\times10^{-7}\right)\left(\frac{T}{M}\right)^{1/2} \tag{9}$$

where M is the molecular weight of the absorbing species. The collisional broadening is characterized by a collisional width $\Delta\nu_c$ [cm^{-1}]. $\Delta\nu_c$ depends on pressure and gas composition, and has unique broadening behavior for every molecular collision partner Y:

$$\Delta\nu_c = P\sum_Y X_Y 2\gamma_{\mathrm{abs}-Y} \tag{10}$$

where $\gamma_{\mathrm{abs}-Y}$ [cm^{-1}atm^{-1}] is the broadening coefficient between collision partner Y and the absorbing species. $\gamma_{\mathrm{abs}-Y}$ is typically modeled using a power law, often expressed in terms of $2\gamma_Y$:

$$2\gamma_Y(T) = 2\gamma_Y(T_0)\left(\frac{T_0}{T}\right)^n \tag{11}$$

in which n is a temperature-dependent exponent. With knowledge of n, $\gamma_Y(T_0)$, T, and P, Eqs. (7) through (11) can be used to determine $\varphi_i(\nu_{i,0})$, which can be used with L and measured $\alpha_{\nu_{i,0}}$ to determine X_{abs} per Eq. (3) when fixing the laser wavelength near the linecenter.

3. Spectral line selection

Line selection for LAS sensing is typically influenced by the strength, isolation, and temperature sensitivity of accessible rovibrational transitions. For multi-isotopologue sensing, relative proximity of transitions for both ^{12}CO and ^{13}CO is also an important consideration. Ideally, the spectral domain should exhibit minimal interference from neighboring ^{12}CO and ^{13}CO lines, but the lines should be in sufficient proximity that they can be accessed within the tuning depth of a single narrowband light source tuned at a high scan rate (to achieve a correspondingly high measurement rate). The strongest absorption in ^{12}CO and ^{13}CO occurs in the fundamental bands centered near 4.65 μm (2150 cm^{-1}) and 4.76 μm (2100 cm^{-1}), respectively, and this mid-infrared domain has recently become accessible with compact, tunable, room-temperature quantum cascade lasers (QCLs) [4,5].

The P-branches of the bands of both ^{12}CO and ^{13}CO contain many strong rovibrational absorption lines that are favorable for low-interference measurements at moderate pressures

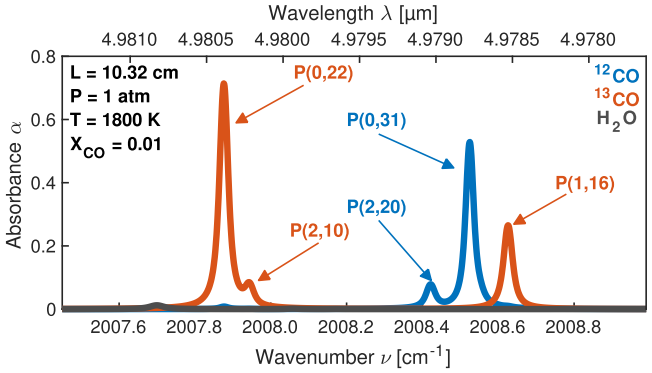

Fig. 2. Examined spectral range noted in Fig. 1 showing the ^{12}CO and ^{13}CO transitions of interest. Absorbance simulated at expected conditions behind a reflected shock with HITEMP 2010 [17].

Table 1
Examined rovibrational transitions in the present work. All linestrengths from the HITRAN database [20] have a reported uncertainty of 2%, except the ^{13}CO P(2,10) and ^{12}CO P(2,20) lines, which have 5% reported uncertainty.

Freq. ν_i [cm^{-1}]	Species	Line (v'', J'')	$S_i(T_0)$ [cm^{-2}/atm]	E_i'' [cm^{-1}]
2007.877	^{13}CO	P(0,22)	$5.56\cdot10^{-3}$	928.582
2007.944	^{13}CO	P(2,10)	$4.20\cdot10^{-15}$	4365.33
2008.422	^{12}CO	P(2,20)	$2.85\cdot10^{-9}$	5051.74
2008.525	^{12}CO	P(0,31)	$6.62\cdot10^{-3}$	1901.13
2008.626	^{13}CO	P(1,16)	$2.50\cdot10^{-6}$	2591.13

($\sim$1 atm) [4,5]. The high-temperature spectra of H_2O, while overlapping those of both CO isotopologues, possesses large spacing between lines in the wavelength domain of the CO isotopologues, offering interference-free spectral windows. Additionally, in the P-branches, there is minimal interference from the high-temperature spectra of both CO_2 isotopologues. A close inspection of the P-branches within 1900–2100 cm^{-1} reveals several isolated absorption features near 2008 cm^{-1} as attractive targets. Figure 2 shows simulated spectra of ^{12}CO and ^{13}CO in this domain of interest along with H_2O at combustion-relevant shock tube conditions using the latest HITEMP [17] database for an optical path-length of $L=$ 10.32 cm, temperatures of $T=$ 1200 K, and mole fractions of $X_{CO}=$ 0.01 and $X_{H_2O}=$ 0.02. The spectra comprises two rovibrational transitions for ^{12}CO and three for ^{13}CO, allowing for multiple two-line thermometry options. For ^{12}CO, the P(31) line in the $v(0\rightarrow1)$ fundamental band provides the dominant contribution, while the P(20) line in the $v(2\rightarrow3)$ hot band contributes more significantly at the higher end of the temperature range. These ^{12}CO lines are also used for measurements in high-temperature, high-pressure rocket engine combustion conditions [21] and atmospheric pressure flames [22,23], and more details about their selection and application can be found in previous work. For ^{13}CO, the strong P(22) line in the $v(0\rightarrow1)$ fundamental band provides the only transition observable at room-temperature for the expected mole fractions, while the P(16) line in the $v(1\rightarrow2)$ hot band contributes more significantly above 600 K. Lastly, the P(10) line in the $v(2\rightarrow3)$ hot band contributes above 1000 K, although this feature blends with the P(22) line at pressures above $\sim$1.5 atm. Table 1 details the ^{12}CO and ^{13}CO rovibrational transitions of interest. A comparison of the different possible combinations of ^{13}CO lines for two-line thermometry using Eq. (5) is shown in Fig. 3. Although ratios including the P(2,10) line show more sensitivity in the higher temperature range, the tendency of this weak line to overlap with neighboring strong lines at low temperatures and higher pressures limits utility.

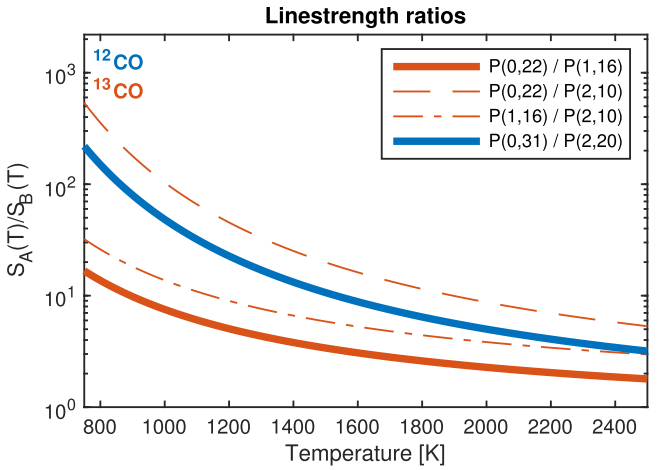

Fig. 3. Calculated linestrength ratios as a function of temperature for the different combinations of the P(0,22), P(1,16), and P(2,10) lines of ^{13}CO and for the P(0,31) and P(2,20) lines of ^{12}CO. Lines used for thermometry in this work are bolded.

Additionally—as discussed in more detail in Appendix A—all the transitions in the domain have linestrength $S_i(T_0)$ uncertainties reported in the HITRAN database [20] as 2%, except the ^{13}CO P(2,10) and ^{12}CO P(2,20) lines, which have 5% reported uncertainty. As a result of these considerations, the P(0,22)/P(1,16) combination with $\Delta E''$=1662.5 cm^{-1} is the most favorable for a wide range of conditions, despite greater line separation in the ^{13}CO spectra. Likewise, owing to its strong absorption over the range of expected temperatures (1100–2200 K) at expected concentrations ($\sim$0.5%), we utilize the ^{13}CO P(0,22) line for high-speed ($>$1 MHz) fixed-DA measurements of ^{13}CO mole fraction.

4. Sensing methodology

This section describes aspects of the sensing methods necessary for successful implementation in the targeted combustion environments. Here we discuss the selection of the light source, laser control and tuning parameters, and the relevant optical setups. We also discuss the spectral data processing methods associated with interpreting the absorbance measurements, including requisite measurements of select line broadening parameters. Estimates of uncertainty regarding all measurements are discussed in detail in Appendix A.

4.1. Optical setup

For the light source, a continuous-wave distributed-feedback (DFB) quantum cascade laser (QCL) (ALPES Lasers) is used to access the two ^{12}CO and three ^{13}CO lines of interest. The QCL is tunable from 2001 to 2014 cm^{-1}, with a typical power of 50 mW at 4.9 µm. In the scanned-wavelength operating mode, a 50 kHz triangle waveform of injection current tunes the QCL across a wavenumber range of $\sim$1.2 cm^{-1} capturing the CO transitions of interest, as depicted in Fig. 4. This effectively yields absorbance area measurements at 100 kHz, counting the up-scan and down-scan. The injection current $i(t)$ is also scanned below the lasing threshold to allow for measurement of the transient thermal emission. The wavelength tuning of the QCL was stable enough to capture the targeted ^{12}CO and ^{13}CO transitions with repeatable signal-to-noise ratios (SNR) from scan to scan. For fixed-wavelength measurements, the injection current is held constant and the QCL is fixed at the linecenter of the ^{13}CO P(0,22) line (2007.8767 $\pm$ 0.00025 cm^{-1}), monitored by a wavemeter (Bristol 671B) before and after each shock tube experiment.

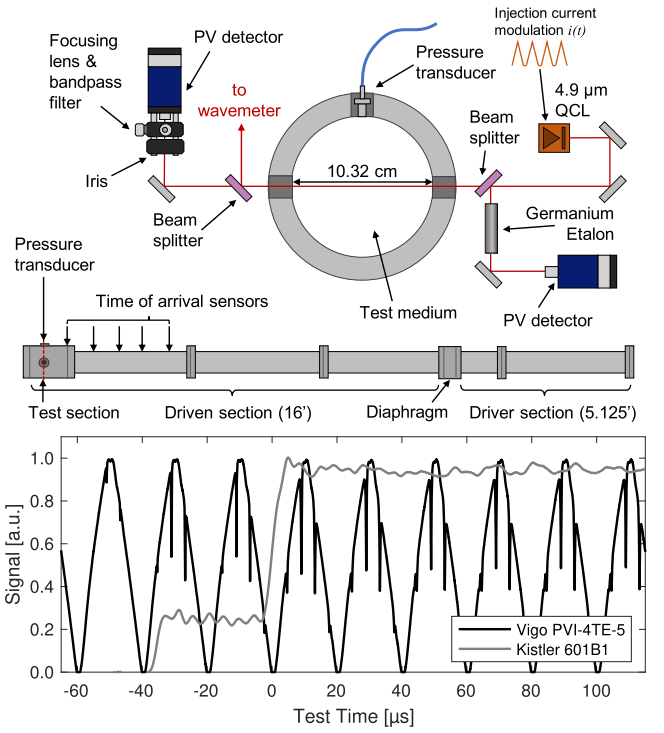

Fig. 4. (Top) Cross-section of the shock tube test section showing windows for optical access and laser/detector setup. (Middle) Side view of the shock tube showing the location of the test section at the end of the driven section of the tube. (Bottom) Example raw detector and pressure transducer signals during non-reactive shock heating of ^{12}CO and ^{13}CO in a He/Ar bath gas.

For light collection, the transmitted laser radiation is passed through a bandpass spectral filter (Spectrogon, 4960 $\pm$ 148 nm) to minimize thermal emission before being focused onto a thermoelectrically cooled photovoltaic (PV) detector (Vigo PVI-4TE-5). For each measurement I_t, a corresponding background I_0 is recorded without a mixture present to establish a baseline for calculation in Eq. (3). For scanned-wavelength measurements, the relative frequency of the laser light is determined using a germanium etalon with a free spectral range of 0.0241 cm^{-1}. For all tests, the detector is sampled at its maximum bandwidth of 15 MHz for an equivalent measurement rate of 7.5 MHz.

4.2. Shock tube experiments

The high-enthalpy shock tube (Fig. 4) used in this work is of a weldless flange design similar to that described by Aul et. al [24]. The shock tube is connected to vacuum pumps, an agitated mixing tank, and a gas delivery manifold used to barometrically prepare the mixtures of interest for all experiments. The test section of the shock tube has an internal diameter of L = 10.32 cm, and is circumscribed by interchangeable ports which can hold sensors or optical windows 2 cm from the end wall. For these experiments, two half-inch sapphire windows are used to allow transmission of the laser light into and out of the tube. A dynamic pressure transducer (Kistler 601B1) is also mounted in one of the ports and records the pressure trace of the incident and reflected shock wave through a charge amplifier (Kistler 5018A). Five time-of-arrival sensors (Dynasen, Inc.) provide a means for determining the incident shock velocity, from which the reflected shock test conditions (T_5, P_5) are determined [25]. Uncertainty in reflected shock temperature and pressure are typically about 1% when properly accounting for vibrational relaxation of all components of the test gas [26].

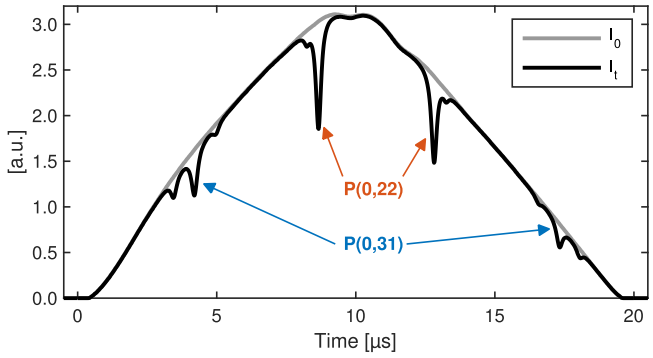

Fig. 5. Example scanned-wavelength detector signal in the shock tube.

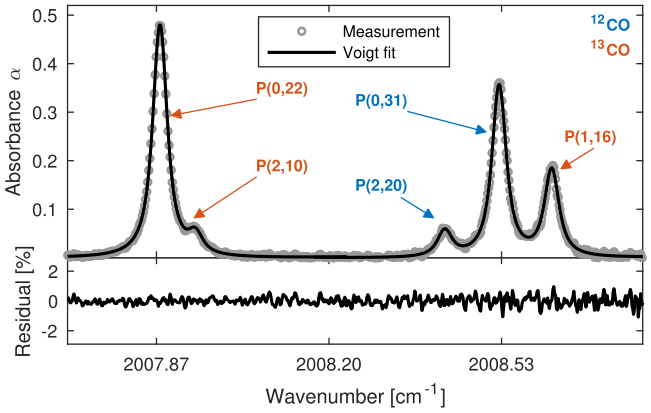

Fig. 6. Example scanned-wavelength Voigt fitting of data in a high enthalpy shock tube experiment.

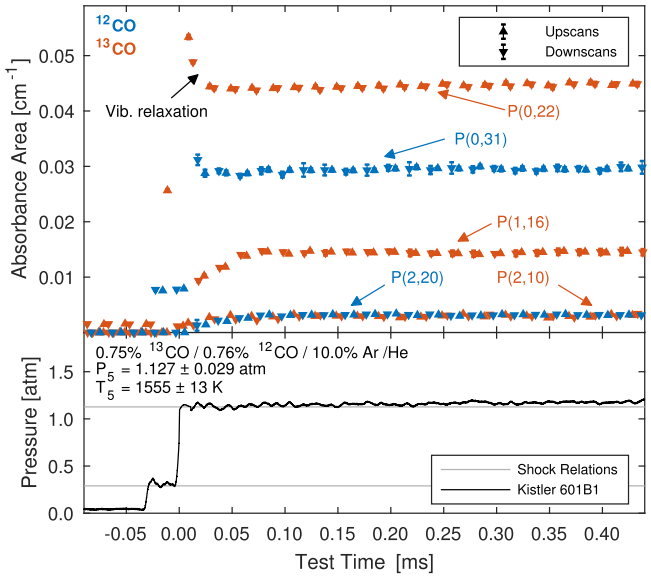

Fig. 7. (Top) Example scanned-wavelength absorbance area measurement during a non-reacting shock of ^{12}CO and ^{13}CO. (Bottom) Pressure time history for corresponding shock.

Once the QCL and detector were aligned and operational, a series of argon (Ar) shocks were performed to ensure that no beam-steering was present, which would complicate the baseline fitting discussed in Section 4.3.1. Data from the detector at 15 MHz using a PicoScope 4000 series data acquisition module, which was triggered to record by the time-of-arrival sensors.

^{12}CO and ^{13}CO thermometry and concentration measurements at 100 kHz were conducted in the shock tube over a range of combustion-relevant temperatures (1100–2300 K) and near-atmospheric pressures (0.5–1.5 atm) using scanned-DA techniques. For the non-reactive thermometry and concentration studies, equal concentrations of ^{12}CO and ^{13}CO were prepared with different bath gas mixtures of argon (Ar) and helium (He) for measurements at temperatures between 1100 and 2300 K. These experiments provided validation of simultaneous ^{12}CO and ^{13}CO thermometry and mole fraction measurement. For reactive studies, mixtures of Ar, O_2, and combinations of $^{12}CH_4$, $^{13}CH_4$, and $^{12}C_2H_4$ were prepared for oxidation experiments at temperatures from 1400 to 1800 K, measured with both scanned-DA and fixed-DA methods. Initial experiments validated the ability of the shock tube to produce repeatable species time-histories in oxidation studies with a fuel (CH_4) that has well-known ignition behavior [27]. Finally, we demonstrated the ability of the sensor to simultaneously resolve production and destruction of both CO isotopologues during ignition of a binary fuel mixture in which one of the fuels was isotopically labeled. These experiments validated the sensor's ability to perform time resolved multi-isotopologue species measurements for combustion studies.

4.3. Data processing

Here we detail the different data processing methods required to infer temperature and mole fraction from both scanned-DA and fixed-DA measurements as they relate to Eqs. (3)–(11). As mentioned, we utilize the Voigt lineshape function to fit the CO spectra for all measurements, and the details of implementing this model for both scanned-DA and fixed-DA measurements are provided in the following subsections.

4.3.1. Scanned-wavelength direct absorption (100 kHz)

Raw detector voltage data, such as those shown in Figs. 4 and 5, are processed using Eq. (3) to obtain spectral absorbance α_ν, such as shown in Fig. 6. The spectral domain is then divided into two regions; the first containing the P(0,22) and P(2,10) lines of ^{13}CO and the second containing the P(2,20) and P(0,31) lines of ^{12}CO and the P(1,16) line of ^{13}CO. A two-line least-squares fitting routine was used for the first region, while a three-line fitting routine was used for the second region. All lines in this work were fit using the Voigt lineshape profile with absorbance area A_i and collisional width $\Delta\nu_c$ as free parameters, while Doppler width $\Delta\nu_D$ was fixed independently using temperatures estimated from ideal shock relations [25]. Residuals from the fitting were all within 2% during the shock tube experiments, confirming the appropriateness of the Voigt lineshape for this study.

Example calculated absorbance areas from a non-reactive shock tube experiment containing $X_{^{12}CO} = X_{^{13}CO} = 0.0075$ are shown in Fig. 7. Some vibrational relaxation is visible immediately after the incident and reflected shocks, but the absorbance area calculations for all transitions are shown to be stable in time subsequently. Moreover, the absorbance areas calculated from the upscan of the triangle wave agree with the absorabance areas calculated from the downscan of the triangle wave, highlighting the ability of the sensor to perform measurements at 100 kHz. As seen in Fig. 7, the P(0,22) and P(1,16) lines of ^{13}CO and P(0,31) line of and ^{12}CO show favorable absorbance area with 0.75% ^{12}CO and ^{13}CO seeded in the bath gas. These absorbance areas are used to infer temperature and mole fraction of both CO isotopologues using Eqs. (5) and (4), respectively, and the results are discussed in Sections 5 and 6.

4.3.2. Fixed-wavelength direct absorption (> 1 MHz)

To enable high time resolution (> 1 MHz) fixed-DA measurements, a spectral model accounting for collisional broadening

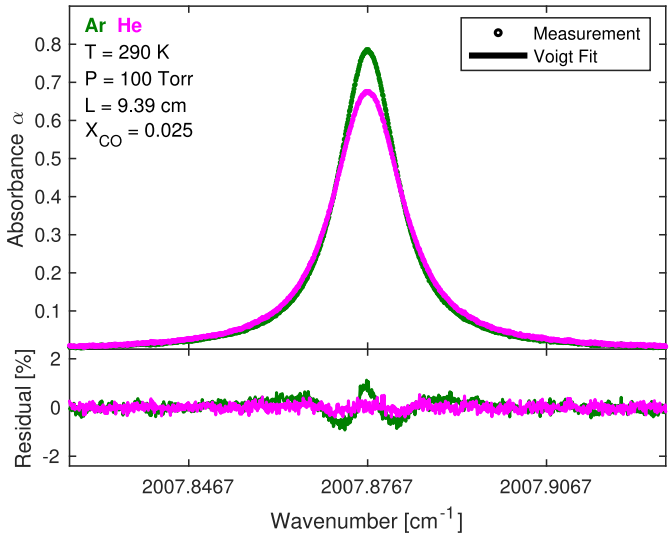

Fig. 8. Example absorbance spectra and spectral fits of the P(0,22) ^{13}CO line for both He and Ar collision partners in a high temperature optical cell.

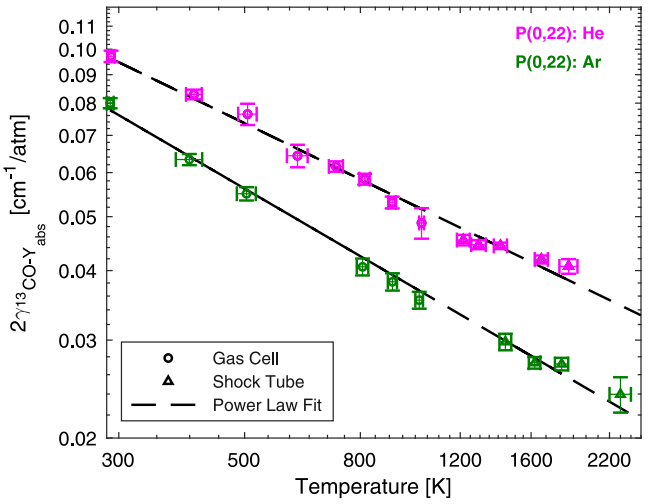

Fig. 9. He- and Ar-broadening coefficients for the P(0,22) ^{13}CO line with power law fits for 300–2300 K. High-temperature gas cell data marked with circles. Data from shock tube measurements marked with triangles.

Table 2
Spectral modeling parameters for the P(0,22) ^{13}CO line.

Y	$2\gamma_{^{13}CO-Y}(T_0)$ [cm^{-1}/atm]	$n_{^{13}CO-Y}$	Range [K]
He	0.0953 ± 0.0023	0.494 ± 0.024	296–1863
Ar	0.0767 ± 0.0017	0.595 ± 0.026	296–2312

(Eqs. (7) through (11)) is necessary to simulate linecenter absorbance, which is then used to infer mole fraction from measured linecenter absorbance using Eq. (3). Our shock tube studies are carried out with He and/or Ar as the bath gas, for which collisional broadening parameters are unavailable in the current HITRAN [20] and HITEMP databases [17]. For the aforementioned scanned-DA measurements, these broadening parameters are not a prerequisite to employ the two-line thermometry methods discussed in Section 2.2, since Eqs. (4) and (5) are independent of the lineshape function $\varphi_i(\nu)$. However, for a given oxidation experiment utilizing fixed-DA, both the broadening parameters $\gamma_Y(T_0)$ and n as well as the temperature of the medium must be known independently to model $\varphi_i(\nu)$ and interpret the absorbance measurements. To determine the He- and Ar-broadening parameters of the P(0,22) line of ^{13}CO, high-temperature ($>$ 1000 K) absorbance measurements were made during the non-reacting shock tube experiments described previously, while lower-temperature (300–1000 K) measurements of broadening parameters for the P(0,22) line of ^{13}CO were taken using a high-temperature optical static cell at pressures varying from 40–100 Torr. The relative temperature and pressure uncertainty in the cell is approximately $\pm$0.3%, and $\pm$0.125%, respectively. More details about the mechanical design and thermal analysis of the cell are available in another work [28]. For the shock tube broadening measurements in Ar, some He was added (10%) to the bath gas to accelerate vibrational relaxation of CO behind the reflected shock wave, necessitating independent knowledge of He broadening parameters.

For measurements in the optical static cell, the QCL was scanned at 70 kHz from 2007.82–2007.96 cm^{-1} to cover the entire P(0,22) line, and data was collected from the detector at 7.5 MHz using a PicoScope 5000 series data acquisition module. Figure 8 shows example scanned measurements of the P(0,22) line using the DFB QCL with both He and Ar as bath gases. Fit parameters were excluded for conditions in which the Voigt fit exhibited large residuals ($>$ 3%), likely due to collisional narrowing [29]. Measurements of broadening coefficients $2\gamma_{^{13}CO-Y}(T)$ of the P(0,22) line from both the shock tube and gas cell experiments of ^{13}CO are shown in Fig. 9. Also shown is a least-squares fit [30] of Eq. (11) to estimate both the temperature-dependent exponents n_{He}, $\gamma_{He}(T_0)$, n_{Ar}, and $\gamma_{Ar}(T_0)$, as well as their respective uncertainties, Δn_{He}, $\Delta\gamma_{He}(T_0)$, Δn_{Ar}, and $\Delta\gamma_{Ar}(T_0)$. The resulting broadening parameters are given in Table 2.

To obtain high-speed measurements of ^{13}CO mole fraction in a reacting mixture, we perform a fixed-DA measurement during the reaction behind a reflected shock as well as a companion scanned-DA measurement with the same mixture composition at the same reflected shock conditions to obtain a temperature time-history using two-line thermometry. Using the measured reflected shock pressure and calculated temperature, as well as the parameters in Table 2 in conjunction with Eqs. (7) through (11), we calculate $\varphi_i(\nu_{i,0})$ using a Voigt lineshape profile [19] and subsequently determine mole fraction from Eq. (3), as shown in Section 6. By accounting for the temperature change in the collisional broadening during the reaction, we reduce the uncertainties associated with the mixture's exothermicity [9], allowing for more accurate measurements of CO mole fraction. Results are provided in Section 6.

5. Validation results

The main objective of this work is to provide the ability for accurate simultaneous temperature and concentration measurements of both CO isotopologues at concentrations sensitive enough to distinguish competitive oxidation between different components of fuel mixtures. This section discusses the performance of the sensor in high-temperature environments typical of shock tube oxidation studies. For a comprehensive uncertainty analysis on the measurements of temperature and mole fraction reported here, the reader is referred to Appendix A.

The temperature for each reflected shock is calculated from the incident shock velocity measured by the time-of-arrival sensors and is treated as the known temperature, while the known mole fractions of both CO isotopologues for non-reacting shocks are calculated from the barometric mixture preparation. Known reflected shock temperature and CO mole fractions are overlaid with measured values during a representative shock tube experiment in Fig. 10, showing excellent agreement. Typical uncertainty in temperature measured using two-line thermometry on the upscan (50 kHz) absorbance areas for each CO isotoplogue is ap-

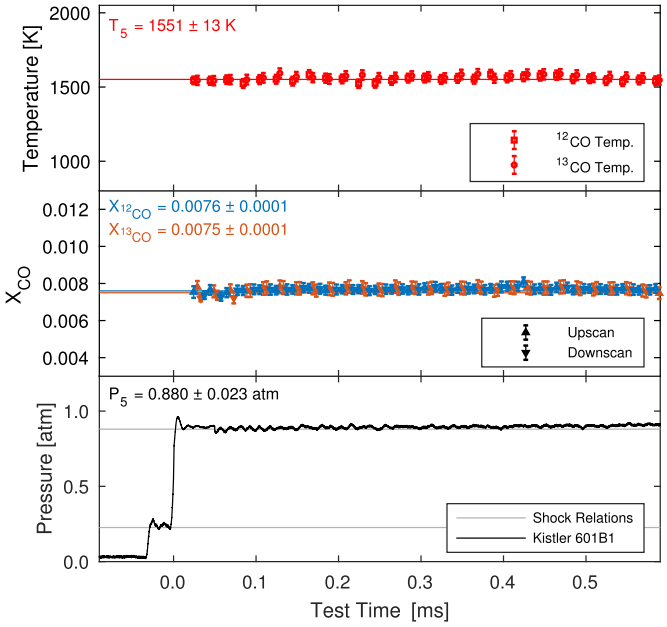

Fig. 10. Measured temperature and mole fraction of ^{13}CO and ^{12}CO based on two-line thermometry for a non-reactive ^{13}CO/^{12}CO/Ar/He shock with comparison to calculations from the ideal shock relations and known mixture concentrations.

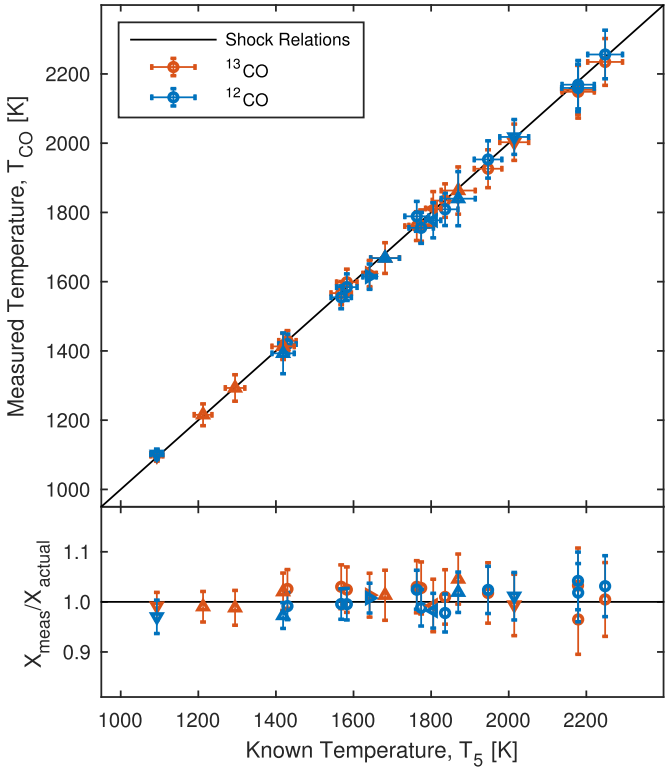

Fig. 11. Comparison of multi-isotopologue thermometry and concentration measurements with known quantities in high-enthalpy shock tube from 1100–2250 K. Different markers indicate distinct ^{12}CO/^{13}CO/Ar/He mixtures.

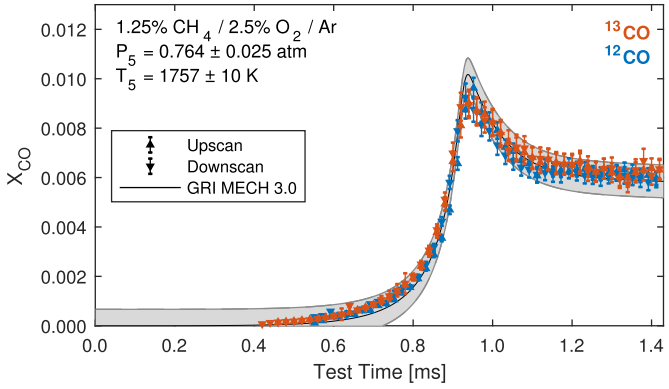

Fig. 12. Mole fractions of ^{12}CO and ^{13}CO from two different shock oxidation experiments using $^{12}CH_4$ and $^{13}CH_4$ as the fuel, respectively. Shaded regions indicate uncertainty in model predictions due to uncertainties in reflected shock conditions.

proximately 2% over the test time ($\sim$1 ms) of the non-reacting shock. It can also be seen that the mole fraction values calculated from the upscan absorbance agrees with those calculated from the downscan absorbance, enabling 100 kHz mole fraction measurements. Several of these experiments were conducted for a temperature range relevant to combustion kinetic studies. The accuracy of the sensor over 1100–2250 K is shown in Fig. 11, in which the measured temperatures and mole fractions of ^{12}CO and ^{13}CO are compared with the expected temperature from shock relations and the concentrations recorded barometrically during mixture preparation. The sensor is shown to reliably determine temperature and mole fraction for various concentrations of ^{12}CO and ^{13}CO in different bath gas mixtures of He and Ar. At lower temperatures ($<$1300 K) and higher pressures ($>$1.5 atm), the P(2,10) line of ^{13}CO and the P(2,20) line of ^{12}CO were too broadened to make reliable measurements of the absorbance areas for those transitions. However, in these conditions, the P(0,22) and P(1,16) line of ^{13}CO and the P(0,31) line of ^{12}CO are still distinguishable enough for thermometry and mole fraction measurements of ^{13}CO, as shown in Fig. 11 for the points at 1200 and 1300 K. Assuming temperature from ideal shock relations, ^{12}CO and ^{13}CO exhibited detection limits of 150 ppm and 160 ppm, respectively, using scanned-DA methods at 1500 K. The corresponding ^{13}CO detection limit using fixed-DA methods was approximately 21 ppm at 1620 K, assuming a 1-σ noise floor.

To validate both the experimental apparatus and the similarities of the reaction rates associated with isotopologues of fuels, we performed shock tube oxidation experiments at approximately the same conditions (nominally $T_5 = 1758 \pm 10$ K and $P_5 = 0.764 \pm 0.025$ atm) for two different stoichiometric ($\phi = 1$) mixtures of 1.25% CH_4 / 2.50% O_2 / 96.5% Ar; one with $^{12}CH_4$ and another with $^{13}CH_4$. The ignition behavior of CH_4 is one of the most well-known among fuels, and for which there are several established kinetic mechanisms; these experiments (at conditions for which much data exists in the literature) serve to validate the measurement technique as well as the facility used to prepare and react the mixtures. The mole fractions of both CO isotopologues from these experiments are shown in Fig. 12, along with a chemical kinetic simulation performed using Cantera [31] with an unmodified GRI-MECH 3.0 mechanism [32]. The mole fraction results of the independent experiments agree with one another and with the kinetic model for methane combustion, highlighting the similarities in ignition behavior of the isotopically labeled fuels. Further discussion regarding the kinetic effects of isotopic substitution is provided in Appendix B.

6. Demonstration results

In order to conclusively demonstrate the ability of the technique to discern competitive oxidation between different components of a fuel mixture, a representative combination of fuels and reflected shock environments must be determined. A well-established and tractable chemical kinetic mechanism, GRI MECH 3.0 [32], was chosen for modification accounting for isotopic

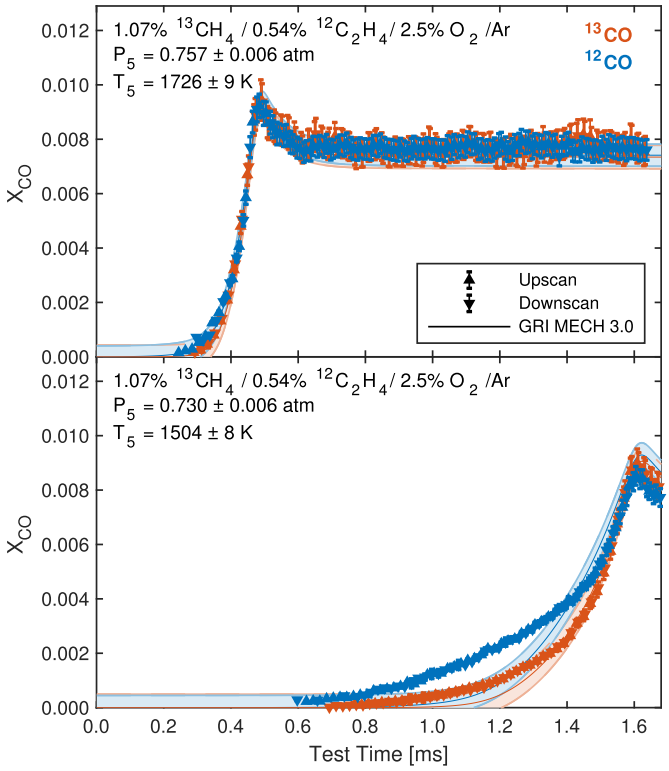

Fig. 13. Measured CO mole fraction during ignition of fuel/O_2 mixture diluted in Ar at 1726 K (top) and at 1504 K (bottom) alongside chemical kinetic predictions. Shaded regions indicate uncertainties in kinetic model due to uncertainty in mixture composition and reflected shock conditions.

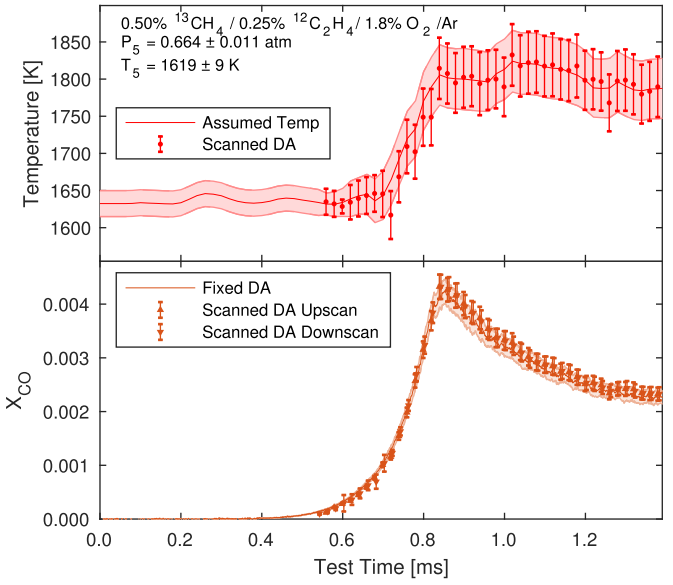

Fig. 14. (Top) Measured (scanned-DA) and assumed (fixed-DA) temperature for oxidation experiments in identical reflected shock conditions. (Bottom) CO mole fraction during scanned-DA (markers) and fixed-DA (smooth line) experiments. Shaded regions indicate fixed-DA uncertainties.

labeling of carbon atoms. We used this modified mechanism to survey and downselect temperature and pressure regimes of interest for ignition of isotopically-labeled fuel mixtures, with particular attention to smaller carbon-number species relevant to real fuel oxidation [11,12]. Owing to all the possible permutations of carbon atoms in the molecules possessing more than one carbon atom, this modification increased the number of species in the mechanism from 53 to 117 and the number of reactions from 325 to 886.

Two fuels with distinctly different structure (and hence, ignition behavior), methane (CH_4) and ethylene (also known as ethene, C_2H_4), were chosen for inclusion in reactive mixtures for the initial competitive oxidation tests. Shock tube oxidation experiments were performed with different mixtures of $^{13}CH_4$, $^{12}C_2H_4$, O_2, and Ar to validate the sensor's ability to measure both species during a reaction. Although known as the simplest hydrocarbon, CH_4 often requires higher temperatures than other hydrocarbons at stoichiometric equivalence ratios to ignite in a comparable amount of time [33,34]. For example, at atmospheric pressure, a temperature of about 1700 K is required for successful ignition within the shock tube test times demonstrated in this work ($\sim$2 ms). The addition of C_2H_4 into the fuel mixture reduces this temperature requirement, and a stoichiometric mixture of 67% CH_4/33% C_2H_4 will ignite at 1500 K within this test time. Notably, this particular ratio of $^{13}CH_4$ to $^{12}C_2H_4$ results in a nearly equal number of carbon atoms corresponding to each carbon isotope.

6.1. Multi-isotopologue CO sensing in reacting mixtures

To specifically test competitive oxidation in oxygen-starved environments, a fuel-rich mixture ($\phi = 1.5$) of 67% CH_4/33% C_2H_4 and O_2 was prepared in an Ar bath gas. Example results in Fig. 13 show the mole fraction results of two scanned-DA experiments with this mixture under similar shock-heated pressures (0.744 ± 0.02 atm) and different temperatures (1726 ± 9 K and 1504 ± 8 K), along with the modified kinetic simulation prediction. It can be seen that at higher temperatures (>1700 K), the time histories of the mole fractions of both ^{12}CO and ^{13}CO are both similar, tracking with one another. This indicates that the carbon atoms from both $^{12}C_2H_4$ and $^{13}CH_4$ are oxidizing at similar rates in these conditions. This particular observation agrees with the modified chemical kinetic prediction quite well. At lower temperatures, however ($\sim$1500 K), a separation of reaction timescales is visible between ^{12}CO and ^{13}CO—^{12}CO appears earlier and in higher quantities than ^{13}CO. This indicates that the carbon atoms from $^{12}C_2H_4$ and $^{13}CH_4$ are oxidizing at different rates in these conditions, at least initially. Moreover, the degree to which the timescales are initially separated is underpredicted by the modified kinetic mechanism, which shows the mole fractions agreeing within the model uncertainty. Notably, the experimental mole fraction results for ^{12}CO and ^{13}CO disagree with one another beyond what is explicable with experimental uncertainty.

6.2. High-speed ^{13}CO sensing

Since high-speed ^{12}CO sensing using transitions in the P-branch of the fundamental band has already been demonstrated by other researchers [4,35], we focus the discussion of our fixed-DA measurements on ^{13}CO. To demonstrate the ability of the sensor to measure mole fraction of ^{13}CO at a time resolution (>1 MHz) suitable for chemical kinetic studies at higher temperatures (>1800 K), a stoichiometric mixture ($\phi = 1$) of 67% CH_4/33% C_2H_4 and O_2 was prepared in an Ar bath gas. Figure 14 shows the mole fraction results of two independent shock tube oxidation experiments—one scanned-DA and one fixed-DA—with nearly identical reflected shock conditions. The two-line thermometry temperature time history from the scanned-DA experiment, shown in red markers with error bars, was used to estimate a temperature time history for the corresponding fixed-DA experiment, shown as a line with shaded error region. The mole fraction results from the fixed-DA measurements show excellent agreement with the results from the scanned-DA measurements,

building confidence in both the precision and versatility of the sensor and in the accuracy of the broadening parameters we report in Table 2.

7. Discussion

In Section 6, we demonstrated the ability of multi-isotopologue laser absorption spectroscopy to unambiguously identify the parent fuel sources of intermediate oxidation species. The technique represents a starting point of a new avenue towards anchoring and constraining detailed reaction mechanisms of fuel mixtures using laser absorption spectroscopy. In many modern kinetic mechanisms in the literature, significant uncertainties exist in several key elementary reactions involved in the production of CO, particularly reactions involving the formyl (HCO) and ketenyl (HCCO) radicals [7,9,36], which we touch on here.

As an example of the type of analysis that can be made with this experimental technique, we performed a reaction pathway analysis using the GRI-MECH 3.0 mechanism [32] modified for isotopic tracking for a constant pressure ideal gas reactor simulation in Cantera [31] for the low-temperature ignition condition in Fig. 13. The reaction pathway analysis yielded some insights into the mechanism potentially responsible for disagreement between the experiment and the model. During the onset of CO formation for both isotopologues ($\sim$1.1 ms in the lower plot of Fig. 13), the primary pathway for the generation of ^{13}CO is through the methyl radical (CH_3) and formaldyhyde (CH_2O):

$$HO_2 + CH_3 \longleftrightarrow OH + CH_3O \quad \text{R119}$$

$$O + CH_3 \longleftrightarrow H + CH_2O \quad \text{R10}$$

$$H + CH_2O + M \longleftrightarrow CH_3O + M \quad \text{R57}$$

$$CH_2O + H \longleftrightarrow HCO + H_2 \quad \text{R58}$$

$$HCO + M \longleftrightarrow H + CO + M \quad \text{R167}$$

For reader convenience, we have labeled the reactions according to their reaction number in GRI MECH 3.0. In the oxidation of C_2H_4, HCO is also comparably produced via direct O atom attack,

$$O + {}^{12}C_2H_4 \longleftrightarrow {}^{12}CH_3 + H{}^{12}CO \quad \text{R25}$$

and, in conjunction with reaction R167, this represents the dominant pathway to CO for C_2H_4 during this stage of the oxidation. Another comparable path to HCO occurs through the reaction of the vinyl (C_2H_3) radical with O_2, a reaction which is known to have many possible pathways [37]:

$${}^{12}C_2H_3 + O_2 \longleftrightarrow H{}^{12}CO + {}^{12}CH_2O \quad \text{R173}$$

These additional pathways to $H^{12}CO$ and ^{12}CO production require $^{12}C_2H_4$ and so are not available to ^{13}CO, because the only ^{13}C in the system must ultimately come from $^{13}CH_4$, and $^{13}CH_3$ recombination and downstream production of $^{13}C_2H_3$ is not competitive under these conditions. It should be noted that at this time ($\sim$1.1 ms), a significant pathway for the vinyl radical reaction with O_2 produces ketene (CH_2CO):

$${}^{12}C_2H_3 + O_2 \longleftrightarrow O + {}^{12}CH_2{}^{12}CHO \quad \text{R294}$$

$$H + {}^{12}CH_2{}^{12}CO + M \longleftrightarrow {}^{12}CH_2{}^{12}CHO + M \quad \text{R304}$$

However, at $\sim$1.1 ms, ketene is not yet reacting appreciably.

A bit later in the reaction ($\sim$1.3 ms in the lower plot of Fig. 13), the aforementioned pathway to CO through the methyl radical and formaldehyde stays dominant for ^{13}CO and becomes dominant for ^{12}CO. Additionally, for the formation of ^{12}CO from $^{12}C_2H_4$, a significant pathway through the ketenyl (HCCO) radical becomes available as ketene undergoes hydrogen abstraction:

$$H + {}^{12}CH_2{}^{12}CO \longleftrightarrow H{}^{12}C{}^{12}CO + H_2 \quad \text{R80}$$

$$H{}^{12}C{}^{12}CO + O_2 \longleftrightarrow OH + {}^{12}CO + {}^{12}CO \quad \text{R176}$$

As with earlier, this CO pathway is unavailable to ^{13}CO, since it ultimately comes from $^{12}C_2H_3$. From these two snapshots in time of the reaction paths for the GRI mechanism, it is clear that there are many more paths to ^{12}CO than to ^{13}CO, and this is validated by our experimental results. Since the results in Fig. 13 show that there is a larger separation of timescales between the appearance of ^{13}CO and ^{12}CO than predicted by the model, however, it is reasonable to suggest that the reaction rates of the pathways exclusive to $^{12}C_2H_4$ should be increased relative to the pathway shared by both $^{12}C_2H_4$ and $^{13}CH_4$.

This reaction analysis on an established kinetic mechanism is an example of how multi-isotopologue laser absorption spectroscopy can provide a unique experimental constraint for efforts to optimize kinetic models of fuel mixtures undergoing competitive oxidation given uncertainties in reaction rate constants [11,12]. Analyses of more modern chemical kinetic mechanisms under active development and optimization are the subject of forthcoming investigations.

8. Summary and potential improvements

A mid-infrared laser absorption sensor was developed for simultaneous temperature and concentration measurements of two CO isotopologues at 100 kHz, enabling novel chemical kinetic studies of isotopically labeled fuel mixtures at combustion-relevant temperatures and near-atmospheric pressures. To the authors' knowledge, these are the first simultaneous time-resolved measurements of multiple CO isotopologues originating from intentionally isotopically-labeled fuels in a reacting mixture. Using the method, we provide initial experimental evidence revealing distinct competitive oxidation in a relevant fuel mixture. In doing so, we also provide the first time-resolved LAS measurements of ^{13}CO for high-temperature shock tube kinetics studies. The technique shows potential to improve understanding of competitive oxidation in multi-component fuel mixtures to distinguish reaction pathways and respective rates by unambiguously identifying the parent fuels of intermediate species. We provide an example of the type of reaction pathway analysis that can be facilitated through use of this method, which can aid combustion kinetics investigations.

To facilitate the use of the sensor in combustion environments in which CO is created and destroyed more quickly than can be satisfactorily measured at 100 kHz, broadening parameter measurements with relevant collision partners He and Ar were conducted and utilized for fixed-DA measurements of the temporal evolution of ^{13}CO at 7.5 MHz, limited only by the bandwidth of the available PV detector (15 MHz). Additional broadening parameters associated with other combustion-relevant species—such as CO_2, H_2O, O_2, and particularly N_2—must be performed before fixed-DA measurements of ^{13}CO can be performed in atmospheric flames or other non-diluted reactive mixtures.

Acknowledgments

All experiments detailed in this work were performed at the Laser Spectroscopy and Gas Dynamics Laboratory at the University of California, Los Angeles, and are supported by the American Chemical Society Petroleum Research Fund (Award No. 59315-DNI6), as well as by the U.S. National Science Foundation, Award

No. 1752516. DIP is supported in part by NSF AGEP Award No. 1306683. FAB acknowledges support from the Eugene V. Cota-Robles Fellowship. KKS acknowledges support from the Department of Defense (DoD) through the National Defense Science & Engineering Graduate (NDSEG) Fellowship Program.

The authors thank Dr. Enoch E. Dames for helpful comments during the preparation of the manuscript. The authors acknowledge the experimental assistance of Ana Y. Contreras in gas cell measurements and optical alignment assistance of Daniel D. Lee. The authors also acknowledge the manufacturing efforts of Nicholas M. Kuenning for several components of the shock tube, supported by the NSF REU Program.

Appendix A. Uncertainty analysis

The uncertainty analysis presented here largely follows that of Wei et al. [23], with added discussion for the transient phenomena associated with shock tube studies. As in that work, unless otherwise noted, we follow the Taylor series method (TSM) of uncertainty propagation [38], in which the uncertainty of a variable r, Δr, is given by:

$$(\Delta r)^2 = \left(\frac{\partial r}{\partial x_1}\Delta x_1\right)^2 + \left(\frac{\partial r}{\partial x_2}\Delta x_2\right)^2 + \cdots \tag{A.1}$$

where x_i are dependent variables and Δx_i are their respective uncertainties.

A1. Temperature uncertainty for scanned-DA

For the two-line thermometry methods used in this work, temperature is given by [19]:

$$T = \frac{\frac{hc}{k_B}(E_2'' - E_1'')}{\ln(R) + \ln\left(\frac{S_2(T_0)}{S_1(T_0)}\right) + \frac{hc}{k_B}\frac{(E_2''-E_1'')}{T_0}} \tag{A.2}$$

Uncertainty in temperature as expressed in Eq. (A.2) depends only on the uncertainties of the reference temperature linestrengths in the HITRAN/HITEMP database, $\Delta S_i(T_0)$, and the uncertainty in the ratio of calculated absorbance areas ΔR:

$$\left(\frac{\Delta T}{T}\right)^2 = \frac{\left(\frac{\Delta R}{R}\right)^2 + \left(\frac{\Delta S_1(T_0)}{S_1(T_0)}\right)^2 + \left(\frac{\Delta S_2(T_0)}{S_2(T_0)}\right)^2}{\left(\frac{hc}{k_B}\frac{E_2''-E_1''}{T_0} + \ln(R) + \ln\left(\frac{S_2(T_0)}{S_1(T_0)}\right)\right)^2} \tag{A.3}$$

The linestrengths of the P(0,22) and P(1,16) lines of ^{13}CO are known to within 2%, and so $\Delta S_i(T_0)/S_i(T_0) = 0.02$ for these lines. For ^{12}CO, the linestrengths of the P(0,31) and P(2,20) lines are known to within 2% and 5%, respectively, and so $\Delta S_i(T_0)/S_i(T_0) = 0.02$ for the P(0,31) line and 0.05 for the P(2,20) line. However, the largest contributor to Eq. (A.3) is usually ΔR, given by the expression:

$$\left(\frac{\Delta R}{R}\right)^2 = \left(\frac{\Delta A_1}{A_1}\right)^2 + \left(\frac{\Delta A_2}{A_2}\right)^2 \tag{A.4}$$

In this work, ΔA_i is conservatively assumed to be equal to the maximum value of the residual multiplied by the absorbance area A_i calculated from the Voigt fitting procedure.

A2. Mole fraction uncertainty for scanned-DA

For the scanned-DA measurements, the mole fraction for any given species is calculated by:

$$X = \frac{A_i}{S_i(T)PL} \tag{A.5}$$

Which is not spectrally dependent on lineshape $\varphi_i(\nu)$. The uncertainty in X depends on the uncertainties of A_i, $S_i(T)$, P, and L:

$$\left(\frac{\Delta X}{X}\right)^2_{\text{SDA}} = \left(\frac{\Delta A_i}{A_i}\right)^2 + \left(\frac{\Delta S_i(T)}{S_i(T)}\right)^2 + \left(\frac{\Delta P}{P}\right)^2 + \left(\frac{\Delta L}{L}\right)^2 \tag{A.6}$$

As mentioned earlier, ΔA_i is calculated based on the residuals of the Voigt fit. The pathlength L of the shock tube is known to a high precision; $\Delta L/L$ is assumed to be much smaller than the other terms in Eq. (A.5) and so it is not included in our uncertainty analysis. However, for the high temperature gas cell, the pathlength changes a small amount with the thermal expansion of the cell, and so $\Delta L = 1$ mm for those experiments.

Uncertainty in pressure, ΔP is dominated by two sources. For all experiments, uncertainty in the pressure transducer / capacitance manometer measurements ΔP_{meas} leads to uncertainties in mole fraction and broadening parameters. For the shock tube experiments, uncertainty in the reflected shock pressure P_5 due to uncertainties associated with the shock relations ΔP_5 contribute.

$$\left(\frac{\Delta P}{P}\right)^2 = \left(\frac{\Delta P_{meas}}{P_{meas}}\right)^2 + \left(\frac{\Delta P_5}{P_5}\right)^2 \tag{A.7}$$

For the sake of brevity, these uncertainties will not be discussed in detail; however, we note that significant contributors to ΔP_5 include uncertainties in the composition of the driven gas (from the barometric mixture preparation), uncertainties in the time-of-arrival measurements, and small uncertainties in the initial pressure P_1 and temperature T_1. Further information can be found in the work by Campbell et al. [26]. This leaves the uncertainty in temperature-dependent linestrength $S_i(T)$, which is given by:

$$S_i(T) = S_i(T_0)\frac{Q(T_0)}{Q(T)}\left(\frac{T_0}{T}\right)\exp\left[-\frac{hcE_i''}{k_B}\left(\frac{1}{T} - \frac{1}{T_0}\right)\right] \times\left[1 - \exp\left(\frac{-hc\nu_{0,i}}{k_BT}\right)\right]\left[1 - \exp\left(\frac{-hc\nu_{0,i}}{k_BT_0}\right)\right]^{-1} \tag{A.8}$$

where Q is the partition function for the molecule of interest, and $\nu_{0,i}$ is the linecenter of the transition i of interest. The two uncertainties we are primarily concerned with are the reference temperature linestrength uncertainty $\Delta S_i(T_0)$ (which we have already calculated) and the uncertainty in temperature-dependent linestrength due to uncertainty in temperature $\Delta S_{i,T}(T)$. In short, ΔT (from the uncertainty in ΔR) affects the $S_i(T)$ used to calculate mole fraction. The following expression can be obtained for the uncertainty in linestrength due to uncertainty in observed temperature, ΔT:

$$\Delta S_{i,T}^2(T) = S_i^2(T)\Delta T^2\left(-\frac{\partial Q(T)/\partial T}{Q(T)} - \frac{1}{T} + \frac{hcE_i''}{k_BT^2} + \frac{hc\nu_{0,i}}{k_BT^2}\left(\frac{\exp\left(-hc\nu_{0,i}/k_BT\right)}{1 - \exp\left(-hc\nu_{0,i}/k_BT\right)}\right)\right)^2 \tag{A.9}$$

This expression is consistent with the analysis presented by Ouyang and Varghese [39]. The total uncertainty in the linestrength $S_i(T)$ can now be calculated:

$$\Delta S_i^2(T) = \Delta S_i^2(T_0) + \Delta S_{i,T}^2(T) \tag{A.10}$$

Thus, all uncertainty dependencies of X as given in Eq. (A.5) are accounted for and ΔX can be calculated using Eq. (A.6).

A3. Mole fraction uncertainty for fixed-DA

For fixed-DA measurements at the linecenter $\nu_{i,0}$, the mole fraction is calculated by:

$$X = \frac{\alpha_\nu}{S_i(T)P\varphi_i(\nu_0)L} \tag{A.11}$$

which is spectrally dependent on lineshape $\varphi_i(\nu)$. The uncertainty in X depends on the uncertainties of α_ν, $S_i(T)$, P, $\varphi_i(\nu_0)$, and L:

$$\left(\frac{\Delta X}{X}\right)^2_{\text{FDA}} = \left(\frac{\Delta\alpha_\nu}{\alpha_\nu}\right)^2 + \left(\frac{\Delta S_i(T)}{S_i(T)}\right)^2 + \left(\frac{\Delta P}{P}\right)^2 + \left(\frac{\Delta L}{L}\right)^2 + \left(\frac{\Delta\varphi_i(\nu_0)}{\varphi_i(\nu_0)}\right)^2 \tag{A.12}$$

The uncertainties ΔP and ΔL remain the same as previously. Since we estimate T from a scanned-DA experiment to calculate both $S_i(T)$ and $\varphi_i(\nu_0)$ for a fixed-DA experiment at nearly identical conditions, the uncertainties $\Delta S_i(T)$ and ΔT also remain the same. Measurement uncertainty in wavelength-dependent absorbance α_ν, as determined by Eq. (3), is influenced by noise in the intensity of the laser light on the detector. We estimate the absorbance uncertainty $\Delta\alpha_\nu$:

$$\Delta\alpha_\nu = -\ln\left(\frac{I_t \pm \Delta I}{I_0 \pm \Delta I}\right) \tag{A.13}$$

where ΔI is the 95% confidence interval associated with the laser and detector noise for both the incident light I_0 and transmitted light I_t, determined from a measurement of I_0 prior to shock heating the test gas. The uncertainty in lineshape $\varphi_i(\nu)$ depends on the spectral model used. As mentioned, we use the Voigt lineshape profile in this work, dependent on Doppler width $\Delta\nu_D$ [cm^{-1}] (which is dependent on temperature T) and collisional width $\Delta\nu_c$ [cm^{-1}]. For brevity, we omit the details of the Voigt profile uncertainty derivation and provide a conservative approximate uncertainty dependence:

$$\left(\frac{\Delta\varphi_i(\nu_0)}{\varphi_i(\nu_0)}\right)^2 = 2\left(\frac{\Delta(\Delta\nu_D)}{\Delta\nu_D}\right)^2 + \left(\frac{\Delta(\Delta\nu_c)}{\Delta\nu_c}\right)^2 \tag{A.14}$$

The uncertainty dependence in the Doppler width $\Delta\nu_D$, $\Delta(\Delta\nu_D)$, can be obtained as:

$$\left(\frac{\Delta(\Delta\nu_D)}{\Delta\nu_D}\right)^2 = \left(\frac{\Delta\nu_{0,i}}{\nu_{0,i}}\right)^2 + \frac{1}{4}\left(\frac{\Delta T}{T}\right)^2 \tag{A.15}$$

where $\Delta\nu_{0,i}$ can be determined by the stability of the wavemeter measurement, in this work ± 0.00025 cm^{-1}. During fixed-DA shock tube studies, collisional width $\Delta\nu_c$ is modeled according to Eq. (10), and the resulting expression for its uncertainty can be calculated:

$$\left(\frac{\Delta(\Delta\nu_c)}{\Delta\nu_c}\right)^2 = \left(\frac{\Delta P}{P}\right)^2 + \left(\frac{\Delta X_Y}{X_Y}\right)^2 + \left(\frac{\Delta\gamma_Y(T_0)}{\gamma_Y(T_0)}\right)^2 + n^2\left(\frac{\Delta T}{T}\right)^2 + (\ln(n)\Delta n)^2 \tag{A.16}$$

The uncertainties in collisional broadening coefficient (in bath gas Y) $\gamma_Y(T_0)$, $\Delta\gamma_Y(T_0)$, and temperature-dependent exponent n, Δn, are determined from the linear regressions applied to Eqs. (10) and (11), respectively, which account for independent measurement uncertainty in multiple dimensions [30]. The mole fraction of the non-reacting bath gas Y (in this work, Ar) is assumed not to change appreciably throughout the experiment, and its uncertainty ΔX_Y is calculated from the barometric mixture preparation. Notably, the temperature-dependent pressure-induced line shift [19] of the ^{13}CO P(0,22) line is not considered when tuning the laser to 2007.8767 cm^{-1}. Assuming $\delta(T_0) = -0.003$ cm^{-1}/atm [40,41] and a temperature-dependent exponent of $M \approx 1$ [42], this results in a line shift of $\delta \approx -0.00035$ cm^{-1} and a $\approx$0.03% underestimation of α_ν at the tested conditions, which is added to the overall uncertainty $\Delta\alpha_\nu$. Thus, all uncertainty dependencies of X as given in Eq. (A.11) are accounted for and ΔX can be calculated using Eq. (A.12).

A4. Ignition delay timing

In the oxidation experiments shown in this paper, the modeled and experimental ignition delay times were observed to occur within the margin of error resulting from the uncertainty in the reflected shock temperature and pressure. Given this agreement, we slightly shift the timing of the modeled results (within the calculated uncertainty) so that the peak CO mole fractions align in time with the experimental results in order to focus comparison on the remainder of the species time-history profiles. In particular this adjustment allows for improved comparison of species evolution/shape before primary ignition.

Likewise, there are small shock-to-shock variations in ignition delay related to the stochastic nature of the diaphragm bursts. The peaks of CO mole fraction and absorbance from the respective scanned-DA and fixed-DA oxidation experiments shown in Fig. 14 were found to agree within the time of one scanned-DA scan, and were similarly synchronized to provide the temperature profile estimate used to determine X_{CO} for the fixed-DA experiment.

Appendix B. Isotopic effects on chemical reactions

In many fields of chemistry, isotopic substitution is used—particularly with hydrogen—for its ability to produce observably different reaction rates as a means to distinguish reaction pathways. In this study, however, we assume that the reaction rates of ^{12}C- and ^{13}C-containing fuels and fuel fragments are indistinguishable enough to have minimal effects on the ignition behavior of the fuels. A brief justification of this assumption follows.

The change in observed reaction rate due to isotopic substitution is related the change in vibrational frequencies of the bonds associated with the transition state of the reaction [13]. The changes in vibrational frequencies are, in turn, dependent on the change in the reduced mass of the atoms in the bonds. As such, reactions involving isotopes of hydrogen have some of the largest observable changes in reaction rates due to its relatively small atomic mass—deuterium has a mass that is twice that of hydrogen, a 100% increase. However, ^{13}C is only 8% more massive than ^{12}C, which has a less significant effect on its respective reduced masses that control the vibrational frequencies of the bonds involved in reactions. An expression for estimating kinetic isotope effects is given in the equation below,

$$\frac{k_{^{12}C}}{k_{^{13}C}} = \exp\left(\frac{hc(\bar{\nu}_{^{12}C} - \bar{\nu}_{^{13}C})}{2k_BT}\right) \tag{B.1}$$

in which k_i is the rate coefficient of a reaction for isotope i, T is temperature, and ν_i is the vibrational frequency associated with the relevant bond to the reaction. For a typical reaction that involves breaking a C-H bond in the stretch coordinate ($\bar{\nu}_{^{12}C} \approx$ 3000 cm^{-1}), substituting ^{13}C ($\bar{\nu}_{^{13}C} \approx$ 2991.10 cm^{-1}) results in a reaction rate ratio $k_{^{12}C}/k_{^{13}C}$ of 1.00493. This assumes the bond is fully broken without any activated complexes (such as would normally exist in a hydrogen abstraction reaction), and so the actual isotope effect will be smaller [13].

This calculation, along with the results shown in Fig. 12, suggest that carbon isotopologues of the fuels in this study can be treated as kinetically indistinguishable, facilitating analysis in chemical kinetic studies utilizing multi-isotopologue laser absorption spectroscopy. Lastly, it should be noted that all the shock tube experiments in this work are carried out with significant dilution ($>96\%$) with small quantities ($<2\%$) of fuels, rendering the effect of naturally occurring ^{13}C during oxidation of ^{12}C-containing fuels negligible.

References

[1] R.K. Hanson, D.F. Davidson, Recent advances in laser absorption and shock tube methods for studies of combustion chemistry, Prog. Energy Combust. Sci. 44 (2014) 103–114, doi:10.1016/j.pecs.2014.05.001.

[2] R.W. Dibble, Laser probing of excited CO products from shock wave initiated oxidation of carbon disulfide, University of Wisconsin, Madison, 1975 Ph.D. thesis.

[3] C.-L. Yu, C. Wang, M. Frenklach, Chemical kinetics of methyl oxidation by molecular oxygen, J. Phys. Chem. 99 (39) (1995) 14377–14387, doi:10.1021/j100039a027.

[4] W. Ren, A. Farooq, D.F. Davidson, R.K. Hanson, CO concentration and temperature sensor for combustion gases using quantum-cascade laser absorption near 4.7 μm, Appl. Phys. B: Lasers Opt. 107 (3) (2012) 849–860, doi:10.1007/s00340-012-5046-1.

[5] R.M. Spearrin, W. Ren, J.B. Jeffries, R.K. Hanson, Multi-band infrared CO_2 absorption sensor for sensitive temperature and species measurements in high-temperature gases, Appl. Phys. B: Lasers Opt. 116 (4) (2014) 855–865, doi:10.1007/s00340-014-5772-7.

[6] W. Ren, R.M. Spearrin, D.F. Davidson, R.K. Hanson, Experimental and modeling study of the thermal decomposition of C_3-C_5 ethyl esters behind reflected shock waves, J. Phys. Chem. A 118 (10) (2014) 1785–1798, doi:10.1021/jp411766b.

[7] Y. Tao, G.P. Smith, H. Wang, Critical kinetic uncertainties in modeling hydrogen/carbon monoxide, methane, methanol, formaldehyde, and ethylene combustion, Combust. Flame 195 (2018) 18–29, doi:10.1016/j.combustflame.2018.02.006.

[8] C.R. Mulvihill, S.A. Alturaifi, E.L. Petersen, High-temperature He- and O_2-broadening of the R(12) line in the $1\leftarrow0$ band of carbon monoxide, J. Quant. Spectrosc. Radiat. Transf. 217 (2018) 432–439, doi:10.1016/j.jqsrt.2018.06.015.

[9] O. Mathieu, C.R. Mulvihill, E.L. Petersen, Assessment of modern detailed kinetics mechanisms to predict CO formation from methane combustion using shock-tube laser-absorption measurements, Fuel 236 (2019) 1164–1180, doi:10.1016/j.fuel.2018.09.029.

[10] S.M. Sarathy, A. Farooq, G.T. Kalghatgi, Recent progress in gasoline surrogate fuels, Prog. Energy Combust. Sci. 65 (2018) 67–108, doi:10.1016/j.pecs.2017.09.004.

[11] H. Wang, R. Xu, K. Wang, C.T. Bowman, R.K. Hanson, D.F. Davidson, K. Brezinsky, F.N. Egolfopoulos, A physics-based approach to modeling real-fuel combustion chemistry – I. Evidence from experiments, and thermodynamic, chemical kinetic and statistical considerations, Combust. Flame 193 (2018) 502–519, doi:10.1016/J.COMBUSTFLAME.2018.03.019.

[12] R. Xu, K. Wang, S. Banerjee, J. Shao, T. Parise, Y. Zhu, S. Wang, A. Movaghar, D.J. Lee, R. Zhao, X. Han, Y. Gao, T. Lu, K. Brezinsky, F.N. Egolfopoulos, D.F. Davidson, R.K. Hanson, C.T. Bowman, H. Wang, A physics-based approach to modeling real-fuel combustion chemistry — II. Reaction kinetic models of jet and rocket fuels, Combust. Flame 193 (2018) 520–537, doi:10.1016/J.COMBUSTFLAME.2018.03.021.

[13] E.V. Anslyn, D.A. Dougherty, Modern Physical Organic Chemistry, University Science Books, 2006.

[14] A. Eveleigh, N. Ladommatos, Isotopic tracers for combustion research, Combust. Sci. Technol. 189 (4) (2017) 660–682, doi:10.1080/00102202.2016.1246440.

[15] P. Ghosh, W.A. Brand, Stable isotope ratio mass spectrometry in global climate change research, Int. J. Mass Spectrom. 228 (1) (2003) 1–33, doi:10.1016/S1387-3806(03)00289-6.

[16] R.H. Michener, K. Lajtha, Stable isotopes in ecology and environmental science, Blackwell Publishing Ltd, Oxford, UK, 2007, doi:10.1002/9780470691854.

[17] L. Rothman, I. Gordon, R. Barber, H. Dothe, R. Gamache, A. Goldman, V. Perevalov, S. Tashkun, J. Tennyson, HITEMP, the high-temperature molecular spectroscopic database, J. Quant. Spectrosc. Radiat. Transf. 111 (15) (2010) 2139–2150, doi:10.1016/j.jqsrt.2010.05.001.

[18] D.A. McQuarrie, J.D. Simon, Physical Chemistry: A Molecular Approach, illustrate ed., University Science Books, 1997.

[19] R.K. Hanson, R.M. Spearrin, C.S. Goldenstein, Spectroscopy and Optical Diagnostics for Gases, Springer, 2016, doi:10.1007/978-3-319-23252-2.

[20] I.E. Gordon, L.S. Rothman, C. Hill, R.V. Kochanov, Y. Tan, P.F. Bernath, M. Birk, V. Boudon, A. Campargue, K.V. Chance, B.J. Drouin, J.M. Flaud, R.R. Gamache, J.T. Hodges, D. Jacquemart, V.I. Perevalov, A. Perrin, K.P. Shine, M.A. Smith, J. Tennyson, G.C. Toon, H. Tran, V.G. Tyuterev, A. Barbe, A.G. Császár, V.M. Devi, T. Furtenbacher, J.J. Harrison, J.M. Hartmann, A. Jolly, T.J. Johnson, T. Karman, I. Kleiner, A.A. Kyuberis, J. Loos, O.M. Lyulin, S.T. Massie, S.N. Mikhailenko, N. Moazzen-Ahmadi, H.S. Müller, O.V. Naumenko, A.V. Nikitin, O.L. Polyansky, M. Rey, M. Rotger, S.W. Sharpe, K. Sung, E. Starikova, S.A. Tashkun, J.V. Auwera, G. Wagner, J. Wilzewski, P. Wcisło, S. Yu, E.J. Zak, The HITRAN2016 molecular spectroscopic database, J. Quant. Spectrosc. Radiat. Transf. 203 (2017) 3–69, doi:10.1016/j.jqsrt.2017.06.038.

[21] D.D. Lee, F.A. Bendana, S.A. Schumaker, R.M. Spearrin, Wavelength modulation spectroscopy near 5 μm for carbon monoxide sensing in a high-pressure kerosene-fueled liquid rocket combustor, Appl. Phys. B 124 (5) (2018) 77, doi:10.1007/s00340-018-6945-6.

[22] C. Wei, D.I. Pineda, C.S. Goldenstein, R.M. Spearrin, Tomographic laser absorption imaging of combustion species and temperature in the mid-wave infrared, Opt. Express 26 (16) (2018a) 20944–20951, doi:10.1364/OE.26.020944.

[23] C. Wei, D.I. Pineda, L. Paxton, F.N. Egolfopoulos, R.M. Spearrin, Mid-infrared laser absorption tomography for quantitative 2D thermochemistry measurements in premixed jet flames, Appl. Phys. B 124 (6) (2018b) 123, doi:10.1007/s00340-018-6984-z.

[24] C.J. Aul, W.K. Metcalfe, S.M. Burke, H.J. Curran, E.L. Petersen, Ignition and kinetic modeling of methane and ethane fuel blends with oxygen: a design of experiments approach, Combust. Flame 160 (7) (2013) 1153–1167, doi:10.1016/j.combustflame.2013.01.019.

[25] J.D. Anderson, Modern Compressible Flow, 3rd ed., McGraw-Hill, 2002.

[26] M.F. Campbell, K.G. Owen, D.F. Davidson, R.K. Hanson, Dependence of calculated postshock thermodynamic variables on vibrational equilibrium and input uncertainty, J. Thermophys. Heat Transf. 31 (3) (2017) 586–608, doi:10.2514/1.t4952.

[27] K. Kohse-Höinghaus, Clean combustion: chemistry and diagnostics for a systems approach in transportation and energy conversion, Prog. Energy Combust. Sci. 65 (2018) 1–5, doi:10.1016/j.pecs.2017.10.001.

[28] K.K. Schwarm, H.Q. Dinh, C.S. Goldenstein, D.I. Pineda, R.M. Spearrin, High-pressure and high-temperature gas cell for absorption spectroscopy studies at wavelengths up to 8 μm, J. Quant. Spectrosc. Radiat. Transf. 227 (2019) 145–151, doi:10.1016/j.jqsrt.2019.01.029.

[29] P.L. Varghese, R.K. Hanson, Collisional narrowing effects on spectral line shapes measured at high resolution, Appl. Opt. 23 (14) (1984).

[30] D. York, N.M. Evensen, M.L. Martnez, J. De Basabe Delgado, Unified equations for the slope, intercept, and standard errors of the best straight line, Am. J. Phys. 72 (3) (2004) 367–375, doi:10.1119/1.1632486.

[31] D.G. Goodwin, R.L. Speth, H.K. Moffat, B.W. Weber, Cantera: An Object-oriented Software Toolkit for Chemical Kinetics, Thermodynamics, and Transport Processes, 2018, doi:10.5281/zenodo.1174508.

[32] G.P. Smith, D.M. Golden, M. Frenklach, N.W. Moriarty, B. Eiteneer, M. Goldenberg, C.T. Bowman, R.K. Hanson, S. Song, W.C. Gardiner, V.V. Lissianski, Z. Qin, GRI-MECH 3.0, http://www.me.berkeley.edu/gri_mech/ 1999.

[33] C.K. Law, Combustion Physics, Cambridge University Press, New York, 2006.

[34] J. Warnatz, U. Maas, R. Dibble, Combustion: Physical and Chemical Fundamentals, Modeling and Simulation, Experiments, Pollutant Formation, 4th ed., Springer, Berlin, Germany, 2006.

[35] R.M. Spearrin, C.S. Goldenstein, J.B. Jeffries, R.K. Hanson, Quantum cascade laser absorption sensor for carbon monoxide in high-pressure gases using wavelength modulation spectroscopy, Appl. Opt. (2014), doi:10.1364/AO.53.001938.

[36] W.K. Metcalfe, S.M. Burke, S.S. Ahmed, H.J. Curran, A hierarchical and comparative kinetic modeling study of C_1–C_2 hydrocarbon and oxygenated fuels, Int. J. Chem. Kinet. 45 (10) (2013) 638–675, doi:10.1002/kin.20802.

[37] C.F. Goldsmith, L.B. Harding, Y. Georgievskii, J.A. Miller, S.J. Klippenstein, Temperature and pressure-dependent rate coefficients for the reaction of vinyl radical with molecular oxygen, J. Phys. Chem. A 119 (28) (2015) 7766–7779, doi:10.1021/acs.jpca.5b01088.

[38] H.W. Coleman, W.G. Steele, Experimentation, Validation, and Uncertainty Analysis for Engineers, 3rd ed., John Wiley & Sons, Inc., Hoboken, NJ, USA, 2009.

[39] X. Ouyang, P.L. Varghese, Line-of-sight absorption measurements of high temperature gases with thermal and concentration boundary layers, Appl. Opt. 28 (18) (1989) 3979, doi:10.1364/AO.28.003979.

[40] B. Sumpf, J.P. Burrows, A. Kissel, H.D. Kronfeldt, O. Kurtz, I. Meusel, J. Orphal, S. Voigt, Line shift investigations for different isotopomers of carbon monoxide, J. Mol. Spectrosc. 190 (2) (1998) 226–231, doi:10.1006/jmsp.1998.7595.

[41] C. Luo, R. Wehr, J.R. Drummond, A.D. May, F. Thibault, J. Boissoles, J.M. Launay, C. Boulet, J.P. Bouanich, J.M. Hartmann, Shifting and broadening in the fundamental band of CO highly diluted in He and Ar: a comparison with theory, J. Chem. Phys. 115 (5) (2001) 2198–2206, doi:10.1063/1.1383049.

[42] R. Wehr, A. Vitcu, F. Thibault, J.R. Drummond, A.D. May, Collisional line shifting and broadening in the fundamental P-branch of CO in Ar between 214 and 324 K, J. Mol. Spectrosc. 235 (1) (2006) 69–76, doi:10.1016/j.jms.2005.10.004.